Extraordinary anisotropic magnetoresistance in math xmlns="http://www.w3.org/1998/Math/MathML">mrow>mi >CaMn/mi>msub>mi mathvariant="normal">O/mi> mn>3/mn>/msub>mo>//mo>mi>CaIr/mi>msub>mi mathvariant="normal">O/mi>mn>3/mn>/msub>/mrow>/ math> heterostructures

Megha Vagadia, Suman Sardar, Tejas Tank, Sarmistha Das, Brandon Gunn, Parul Pandey, R. Hübner, Fanny Rodolakis, Gilberto Fabbris, Yongseong Choi, Daniel Haskel, Alex Frano, and D. S. Rana

Phys. Rev. B **105**, L020402 — Published 3 January 2022

DOI: 10.1103/PhysRevB.105.L020402

Extraordinary anisotropic magnetoresistance in $CaMnO_3/CaIrO_3$ heterostructures

Megha Vagadia[†1], Suman Sardar[†1], Tejas Tank[1], Sarmistha Das[2], Brandon Gunn[2], Parul Pandey[3], R. Hübner[3], Fanny Rodolakis[4], Gilberto Fabbris[4], Yongseong Choi[4], Daniel Haskel[4], Alex Frano[2], and D.S. Rana[*1]

[1]*Department of Physics, Indian Institute of Science Education and Research Bhopal, M.P. 462066, India*

[2]*Department of Physics, University of California, San Diego, CA 92093, USA*

[3]*Institute of Ion Beam Physics and Materials Research, Helmholtz-Zentrum Dresden-Rossendorf, 01328 Dresden, Germany*

[4]*Advanced Photon Source, Argonne National Laboratory, Argonne, Illinois 60439, USA*

Abstract

The realization of four-fold anisotropic magnetoresistance (AMR) in novel 3d-5d heterostructures has boosted major efforts in antiferromagnetic spintronics. However, despite the potential of incorporating strong spin-orbit coupling, only small AMR signals have been detected thus far, prompting a search for new mechanisms to enhance the signal. In this study, we demonstrate an extraordinarily elevated four-fold anisotropic magnetoresistance of 70% realized in $CaMnO_3/CaIrO_3$ thin film superlattices. We find that the bi-axial magnetic anisotropy, and the spin-flop transition in a nearly Mott insulating phase form a potent combination, each contributing one order of magnitude to the total signal. Dynamics between these phenomena capture a subtle interaction of pseudospin coupling with the lattice and external magnetic field; an emergent phenomenon creating opportunities to harness its potential in antiferromagnetic spintronics.

[†]These authors contributed equally.

[*]*E-mail:* dsrana@iiserb.ac.in

The recent emergence of antiferromagnetic (AFM) spintronics over its ferromagnetic (FM) counterpart is inspired by several advantages such as lack of stray fields, low operational power, and ultrafast control of the staggered spins at terahertz frequencies. An AFM spintronic device uses the phenomena of current-induced spin-orbit torque and anisotropic magnetoresistance (AMR) for data writing and reading operations [1-6]. The ongoing efforts in AMR aim to design heterostructures wherein one of its constituents possesses pronounced spin-orbit coupling and magneto-crystalline anisotropies. A coupling of the magnetic field and weak magnetic moments of the canted AFM phase allows these anisotropies to manifest as anisotropic transport. A host of such functionalities are being realized in 3d-5d oxide heterostructures [7-13]. Epitaxial superlattices of iridium oxides (Ca/$SrIrO_3$) having large spin-orbit coupling (SOC) and electron correlation dominated 3d oxides, for example, exhibit emergent magnetic and topological properties wherein the AMR is traced to the anisotropies in their magnetic order [12,13].

The non-magnetic ground state of Ir pseudospin moments (J_{eff} = 1/2) in $SrIrO_3$ and $CaIrO_3$ is defined by the intricate interplay of SOC and electron correlations (U) [7-10]. Tilting the balance of these energetics alters their ground state. For instance, lowering the dimensionality in epitaxial engineered thin films increases the "U" and induces pseudospin-based emergent magnetism. AMR in these iridate heterostructures is pinned to magnetic anisotropies underneath such that uniaxial and biaxial symmetries translate into two-fold and four-fold AMR oscillations, respectively. The latter is preferred due to the larger number of sensitive nodes relevant in efficient data readout. The large-bandwidth $SrIrO_3$ interfaced with magnetic or non-magnetic 3d systems yields two- and four-fold-AMR attributed to a variety of magnetic phases, interface coupling, charge-transfer across the interface, and Rashba SOC [11-13]. In the case of superlattices of low-bandwidth $CaIrO_3$ and $SrTiO_3$, the mechanism underlying the AMR is a combination of in-plane biaxial magnetic anisotropy, magneto-elastic coupling, and interlayer exchange coupling based on tilted oxygen octahedra with glazer notation ($a^-a^-c^+$) across the constituent layers [13, 14-15]. Despite all these diverse yet concerted efforts, the maximum amplitude of the four-fold AMR signal in 3d-5d heterostructures is limited to one percent. This demands the development of novel strategies in terms of the choice of constituents and the architecture of the heterostructures that efficiently translate the magnetism into a larger AMR effect.

Here, we have formed superlattice heterostructures of low bandwidth $CaIrO_3$ and severely distorted canted AFM $CaMnO_3$, where both these constituents have the same sense of oxygen octahedra tilts ($a^-a^-c^+$) - a conducive factor for interlayer coupling. Thus, a thickness-optimized architecture exhibits an unprecedented four-fold AMR of ~70%. Two different effects – bi-axial anisotropy and spin-flop transition - combine to yield this AMR. The former contributes up to 20% signal as 4-fold symmetric sinusoidal AMR and the latter further increases it by an order of magnitude as well as imposes another unique four-fold symmetric component.

The superlattices $[(CaMnO_3)_x/(CaIrO_3)_y]_z$ (x, y = number of unit cells (u.c.)/period; z = repetitions) were prepared by reflection high-energy electron diffraction (RHEED) assisted pulsed laser deposition technique. These samples are labeled as $(MIxy)_z$, where M and I refer to $CaMnO_3$ and $CaIrO_3$ layers, respectively, and categorized based on the period of constituent layers. Details of sample synthesis and characterization methods are appended in Supplemental Material [16].

Magnetization (M) versus temperature and magnetic field (H) data of $(MIxy)_z$ (x = y = 2-4) superlattices are plotted in Fig. 1 (a and b). The magnetic transition temperature (T_C) and the saturation magnetic moment (M_{sat}) decrease with increasing period. A discernible T_C of ~100 K for $(MI22)_{10}$ decreases to ~ 60 K for $(MI44)_5$ and vanishes for higher periods superlattice $(MI84)_5$. In M-H data, a M_{sat} of ~0.4 μ_B/f.u. for $(MI22)_{10}$ agrees well with the reported canted AFM state in $CaIrO_3/CaMnO_3$ heterostructures [13, 17] [Fig. 1(b)]. Given that M_{sat} of the same order manifests in other samples too, the exchange-bias fields (H_{EB}) were measured by performing field-cooled M-H measurements. Observation of an H_{EB} field of 3, 15, 50, and 35 Oe for $(MI22)_{10}$, $(MI33)_5$, $(MI44)_5$, and $(MI84)_5$, respectively, suggests FM and AFM type phases in these superlattices [Fig. 1(c)]. The sheet resistance increases with decreasing $CaIrO_3$ period [Fig. 1(d)]. A sharp upturn in resistivity below 50 K is associated with the Mott-state, which has been explained in the framework of dimensionality-induced enhancement in correlations "U" and charge transfer across the interface [18, 19]. Though all the superlattices are in Mott –insulating regime, the resistivity of $(MI84)_5$ and $(MI44)_5$ is lower than $CaIrO_3$ 10 nm film. As $CaMnO_3$ is an insulator while $CaIrO_3$ is a semimetal, this lesser resistivity can be explained in context to the larger charge transfer in thicker superlattices promoting double exchange in manganite layer [Discussed later].

In superlattices involving manganites, the valence state can be altered at the interfaces through the transfer of charge [20-23]. To explore the microscopic origin of the magnetization and exchange-bias fields in $CaIrO_3/CaMnO_3$ superlattices, the interfacial charge transfer and electronic structure close to the Fermi level were qualitatively visualized via the x-ray absorption spectroscopy (XAS) at the Mn and Ir L-edges [Figs. 2(a)-(b)]. Superlattices with 2 u.c. of one constituent and more than 4 u.c. of the other constituent were chosen to extract the role of both the constituents on charge transfer. The Mn 2p core spectra for all superlattices show a shift in the L_3 edge peak toward lower energy. This suggests the presence of Mn^{3+} ions [18, 24-26], presumably formed by the transfer of charge from the Ir at the interface. Similarly, the XAS at the Ir L-edge spectra depicts a shift in the peak toward higher energy values with respect to IrO_2 reference. This implies that the average Ir valency is more than +4 due to the charge transfer with Mn [27-28]. A nearly constant shift in Ir edge for all superlattices suggests that $CaIrO_3$ tends to lose only a constant fraction of its charge, *i.e*, superlattices with thinner $CaMnO_3$ layers will receive a large fraction of electrons compared to their counterparts with thicker layers. This electronic reconfiguration at the interface is consistent with the emergence of an anomalous magnetism in the superlattices with 2 u.c. of $CaMnO_3$ (See Fig. S4 in Supplemental Material [16] for more details). These data further suggest that the charge transfer depends on the number of both $CaIrO_3$ and $CaMnO_3$ layers (and available carriers) and is related to the trends in electrical transport and magnetization of these samples, as explained below.

$CaMnO_3$ with a severely distorted lattice has a strong affinity for electrons due to its vacant e_g orbital near the Fermi level. A study on Ce^{4+}-doped $CaMnO_3$ revealed that 2–4% electron doping at the Mn-site cants the AFM lattice by 8° and increases the magnetic moments by more than one order of magnitude [29]. This electron doping is similar to charge-transfer/electron leakage across the interface as reported in $CaRuO_3/CaMnO_3$ heterostructures. Here, the electron leakage into $CaMnO_3$ decays exponentially from the interface to within the layer [30-33]. As a result, a fraction of Mn^{4+} proportional to electron leakage converts to Mn^{3+} which induces a double-exchange governed largely canted AFM or a weak FM phase at the interface layer. The inner part $CaMnO_3$ layer remains weakly canted as it coincides with the exponential tail of electron leakage. Both theory and experiments agree on the formation of such a magnetic gradient across the $CaMnO_3$ layer [30-33]. The $CaIrO_3$ too presents a canted AFM phase in low dimensions when hetero-interfaced with a distorted lattice as in 3d-5d

heterostructures. All these reports as well the magnetization data of present $CaIrO_3/CaMnO_3$ samples point towards a canted AFM state for both the constituent layers. The manifestation of H_{EB} in these samples [fig 1(c)] further confirms the magnetic gradient across the interface. An illustration of the direction of canting and moments is presented in Figure 2 (c). The choice of canting the moments in the '*ab*' plane (or in-plane) will be discussed in the context of AMR results in later sections.

AMR was measured in three different senses of rotation of the magnetic field with respect to the superlattice plane [34] and calculated as

$$\text{AMR} = \frac{\rho[B(angle)] - \rho[B(angle = 90^{\circ})]}{\rho[B(angle = 90^{\circ})]} \quad (1)$$

Fig. 3(a) depicts three rotation angles, namely ϕ, θ, and γ with H rotating in xy, yz and zx planes respectively. A comparison of the ϕ-, θ-, and γ-*AMR* for $(MI22)_{10}$ and $(MI33)_5$ is elucidated in Fig. 3 (b)-(c). ϕ-AMR exhibits well-defined four-fold sinusoidal oscillations for both these samples. The θ- and γ-AMRs are two-fold for $(MI22)_{10}$ but have a subtle four-fold component superimposed on a dominant two-fold component for $(MI33)_5$. The origin of the AMR can be ascertained by comparing these three types and analyzing their dependence on the magnetic field. None of the ϕ-, θ-, and γ-AMRs follows a quadratic dependence on B (Fig. S5 [16]), which rules out their origin in Lorentz scattering [13]. In addition, a coincident magnitude and phase of θ- and γ-AMRs for $(MI22)_{10}$ discards the possibility of either spin-Hall MR or s-d scattering as the underlying mechanisms [34-37].

While large θ- and γ-AMRs of up to ~15% manifest for $(MI22)_{10}$, the most remarkable facets of this work are unraveled in much-desired four-fold ϕ-AMR. Fig 3 (d-e) shows the ϕ-AMR as a function of layer thickness and their temperature dependences in $(MIxy)_z$ (x = y = 2-4) and $(MI84)_5$. The $(MI22)_{10}$ exhibits ϕ-AMR of 70% at 10 K. It reduces to ~3–4% for $(MI33)_5$ and further declines to 1% and 0.04% for $(MI44)_5$ and $(MI84)_5$, respectively [Fig. 3(e)]. For all the samples, the AMR decreases with increasing temperature and completely disappears around their T_C in the range of 70-100 K [Fig. 3(e)]. ϕ-AMR of 70% in $(MI22)_{10}$ is unique as: i) it is about two orders of magnitudes larger than reported so far in any 3d-5d heterostructures, ii) it is the largest in complex oxide heterostructures, iii) it falls by two orders of magnitude as the

period (x = y) increases from 2 to 4. This unusual sensitivity of AMR to the constituent layer thickness points toward a different phenomenon promoting the interlayer coupling.

To further pin down the role of individual layers, the ϕ-AMR of $(MIx2)_z$ [x = 4, 6, and 8] and $(MI2y)_z$ [y = 4 and 5] set of heterostructures was studied and the results are presented in the Supplemental Material [16] (Figs. S6, S7 & S8). For the former set, the AMR falls in the narrow range of 0.3–0.6% for all values of 'x' while for the latter set, it drops from 1.6% for y=4 and 0.8% for y=5. These values are much smaller than the ϕ-AMR of 70% for $(MI22)_{10}$. Hence, it is inferred that a two u.c. thickness of both $CaIrO_3$ and $CaMnO_3$ layers is critical to obtain a large AMR. A weak magnetism in the canted AFM phase of these superlattices suggests the origin of the AMR to be the domain scattering based on biaxial magnetic-anisotropy [13, 38-40], which is controlled by the interlayer coupling [41-42]. The strength of this coupling depends on the dimensions of the constituent layers and the interface coupling. In the present case, for example, such coupling is stronger in samples with smaller periods, as in $(MI22)_{10}$. The origin of in-plane biaxial anisotropy and interlayer coupling can be understood as follows.

The inter-and intra-layer magnetic interaction in $CaIrO_3$ layers can be written as [43-44]

$$H_{ij} = J_{ij}\,\vec{S_\iota}\cdot\vec{S_J} + \Gamma_{ij}\,S_i^z S_j^z + \overrightarrow{D_{\iota J}}\cdot[\vec{S_\iota}\times\vec{S_J}] \qquad (2)$$

where J_{ij} is the isotropic Heisenberg exchange, Γ_{ij} is a symmetric traceless second-rank tensor that describes the symmetric portion of the exchange anisotropy and D_{ij} defines Dzyaloshinskii–Moriya (DM) anisotropy. The asymmetric exchange DM interactions with D vector pointing along c-axis (out-of-plane) cants the moments in '*ab*' in-plane along [100]/[010] direction. The latter two terms are essential for in-plane magnetic anisotropy responsible for the manifestation of ϕ-AMR [41-43]. Though originally proposed for layered Sr_2IrO_4 to explain the strength of interlayer coupling between $SrIrO_3$ layers separated by non-magnetic SrO layers, equation (2) is also relevant for superlattices where $CaIrO_3$ or $SrIrO_3$ layers are separated by magnetic or non-magnetic layers [13, 19]. In present $CaIrO_3/CaMnO_3$ superlattices, the $CaIrO_3$ period possesses a larger "U" and a canted AFM phase in low dimensions. The $CaMnO_3$ too is a canted AFM in the same dimensions. In addition, both these layers have a similar sense of structural distortion of (a^-,a^-,c^+) type in low dimensions. This combination of similarity of magnetic phase and structural distortion is a unique attribute, and can be argued as a decisive factor for a strong interlayer

coupling. This, as stated earlier, is responsible for the biaxial anisotropy and a large 4-fold sinusoidal AMR of $CaIrO_3/CaMnO_3$ heterostructures.

Now we turn our attention to some other dynamics of ϕ-AMR which are beyond the contribution of biaxial anisotropy in $(MI22)_{10}$. To relate the AMR with crystal orientations, we present in figure 4 (a) the set of (100) and (110) families of axes along with their labeling in the *'ab'* plane. The sinusoidal ϕ-AMR oscillations in the range of 25-100 K (Fig. 4 (b)) develop some unique features below 22 K. As scrutinized in very close intervals in the range of 10 - 22 K, we observe an additional four-fold pattern of AMR kinks superimposed on the sinusoidal pattern while traversing from the *<100>* to the *<110>* family of crystal axes [Fig. 4 (c)]. A well-defined four-fold ϕ-AMR at 25 K develops a multitude of kinks at 22 - 18 K, followed by symmetric and sharp four-fold kinks at 15 K. A smooth pattern appears at 14 K which further transforms to a sharp step-like pattern at 10 K along with a reversal in polarity of peak amplitude. This unprecedented *ϕ-AMR* behavior is complex both in its pattern and amplitude. In a system with biaxial anisotropy, the trough and crest of the *ϕ-AMR* are assigned to the scattering by soft *<100>* (low resistance) and hard *<110>* axes (peak resistance), respectively. There appears to be a transition in the scattering strength from the *<110>* family of directions at 25 K to the *<100>* directions at 14 K [second panel of Fig. 4(c)]. At 25 K, the uneven amplitude of the crests suggests an uneven scattering from the *<110>* family of hard directions, *i.e,* a larger scattering along A' *[110]* and C' *[−1−10]* compared to B' *[−110]* and D' *[1−10]* [marked by a black dashed line in the second panel of Fig. 4(c)]. In contrast, nearly the same magnitude of troughs suggests the uniform scattering from the *<100>* and *<010>* soft directions (marked by blue dashed lines). At 14 K, however, this behavior reverses. Here, the *<100>* family of soft axes exhibit non-uniformity in the troughs (shown by red dashed lines). This reversal in non-uniformity of scattering is related to a systematic pattern of ϕ-AMR kinks in the transition temperatures [Figs. 4 (c)]. This anomalous AMR of $(MI22)_{10}$ can be explained to arise from competition between pseudospin-lattice (S-L) coupling and field-pseudospin coupling.

The S-L coupling in iridates is given by [41]

$$H_{s\text{-}l} = \Gamma_1 \cos(2\alpha)(S_i^x S_j^x - S_i^y S_j^y) + \Gamma_2 \sin(2\alpha)(S_i^x S_j^y + S_i^y S_j^x) \quad - \qquad (3)$$

Γ_1 and Γ_2 denote the energy scales of S-L coupling to the distortions along *<100>* and *<110>*, respectively, and $\alpha$is the angle between staggered moments and the *<100>* direction. The competition between *xy* and x^2-y^2 quadruple symmetries provides two solutions for H = 0; $\alpha = 45°$ for $\Gamma_1 > \Gamma_2$, and $\alpha = 0$ for $\Gamma_1 < \Gamma_2$. The former is observed in Sr_2IrO_4 and $SrIrO_3/SrTiO_3$ superlattice, while the latter manifests for $CaIrO_3/SrTiO_3$ heterostructures. The ϕ-AMR phase in present superlattices lags by 45° when compared to Sr_2IrO_4 and $SrIrO_3/SrTiO_3$ superlattice [45, 13]. The phase lag in $SrIrO_3$ and $CaIrO_3$-based superlattices is due to the different sense of octahedral rotations in their low-dimensional limits. The solution to the present superlattices is at $\alpha = 0$, as the minimum of AMR oscillation occurs along the *<100>* directions, similar to that in $CaIrO_3/SrTiO_3$ superlattices.

The S-L coupling is strong in the vicinity of a magnetic transition and weakens on lowering the temperature [41, 44]. The *ϕ-AMR* in $CaIrO_3/SrTiO_3$ superlattices is reported to scale with the strength of S-L coupling and thus peaks around the transition temperature. Contrary to this, in $CaIrO_3/CaMnO_3$ superlattices, the ϕ-AMR peaks well below the magnetic transition; for thin superlattices $(MI22)_{10}$ and $(MI33)_5$ AMR amplitude monotonically increases with decreasing temperature showing the maximum AMR at much lower than the magnetic transition i.e. 10 K. For thick $(MIx2)_z$ (x = 4, 6, and 8) superlattices, however, the AMR peaks at the slightly elevated temperature range of 30–50 K (Fig. S9 [16]). This indicates a dominant role of field-pseudospin coupling in addition to the S-L coupling. As the in-plane axis rotates with respect to the field in *ϕ-AMR* measurement, the field-lattice coupling rotates the orthorhombic distortion [41-42]. At low temperatures, however, the stiffness of the lattice weakens the S-L coupling. This tilts the balance in favor of field-pseudospin coupling in the presence of large magnetic moments. A temperature-dependent competition between these two couplings determines the ϕ-AMR for $(MI22)_{10}$ as (i) re-orientation of moments via S-L coupling at high temperature, and (ii) direct coupling of field-spins at low temperature when the lattice is rigid but possesses larger moments. For the superlattice having larger canted pseudospin moments, say for $(MI22)_{10}$, the transition from (i) to (ii) onsets at 25 K. Below this temperature, the AMR increases significantly as evidenced by kinks and sharp steps. These features represent lower resistance and higher magnetization compared to those corresponding sinusoidal AMR along the soft *<100>* axes. Such a state in AFM/canted AFM can be induced by a spin-flop metamagnetic

transition in high magnetic fields [46] [Fig. 4 (d) & Fig. S10 [16]]. These kinks become more pronounced upon lowering the temperature from 22 to 15 K while retaining an overall sinusoidal envelope emerging from the S-L coupling. Eventually, at 10 K and in a high field of 9 T, the ϕ-AMR oscillations reverse their phase by 45°. This is highlighted by the vertical dashed lines matching the *ϕ-AMR* at (i) 14 and 10 K in a field of 9 T [Fig. 4(c)], and (ii) 10 K in fields of 5 T and 9 T (Fig. S11 [16]). The comparison reveals that as the component of the field gets stronger along *<110>*, a spin-flop metamagnetic transition induces a giant ϕ-AMR. The balance shifts dominantly in favor of field-pseudospin coupling that prevents the restoration of the originally sinusoidal resistance.

Metamagnetic transitions are known to occur in manganites as well as in iridates [41, 43, 47-48]. In half-doped manganites, a sharp step-like metamagnetic transition melts an AFM charge-ordered insulating state into a FM metallic state. There are either single- or multiple-step-like metamagnetic transitions that are facilitated via large A-site quenched disorder or slight B-site doping or structural defects. In iridates, dimensionality- and lattice-distortion-dependent metamagnetic transitions have been demonstrated in layered systems [41, 43]. For example, in Sr_2IrO_4, a spin-flop metamagnetic transition is found to be a function of the S-L coupling energetics [41]. A stronger interlayer coupling is the theoretical basis of the spin-flop transition since the coupling strength changes from Sr_2IrO_4 to $Sr_3Ir_2O_7$ [43]. In the present $CaIrO_3/CaMnO_3$ superlattices, the resistance oscillations arise from an oscillating magnetic moment with respect to crystallographic axis embedded in a system with in-plane biaxial magnetic anisotropy. The sharp kink- and step-like transitions are superimposed on these oscillations-inducing an additional large component *ϕ-AMR*-have their origin in spin-flop metamagnetic transition. A relation of the pseudospin arrangement perceived to corroborate with the crest and trough of sinusoidal AMR and the spin-flop AMR is illustrated in figure 4(e). The canting angle and magnetic moment increase upon application of a field of 9 T along (100) easy axis. The canting effect is subtle for field along (110) hard axes [for brevity, the AFM spin arrangement is rotated along the direction of the field]. Larger canted moments along (100) translate into smaller resistivity compared to that along (110) family of hard axes. A spin-flop transition at 10 K in a field of 9 T is also illustrated in figure 4(e). In this case, larger moments of the spin-flop phase are responsible for a large kink/step-like large AMR.

Finally, we emphasize that the choice of the 3d compound is the key to yielding the effective interlayer coupling and distortion required to tune a large ϕ-AMR. In the case of the $CaIrO_3/SrTiO_3$ superlattices, the (a^-,a^-,c^+) octahedral distortions in the $CaIrO_3$ layers propagate into the mediating $SrTiO_3$ layer, provided the $SrTiO_3$ layer consists of only one unit cell [13]. In contrast, in the present $CaIrO_3/CaMnO_3$ superlattices, this distortion propagates into the mediating $CaMnO_3$ layer as thick as eight u.c. In the dimensional limit of a few unit cells, both $CaMnO_3$ and $CaIrO_3$ are orthorhombically distorted with the same octahedral rotation pattern (a^-,a^-,c^+) and similar in-plane DM-type canted AFM phase [13, 49]. This structural similarity between the two constituents enhances the $CaIrO_3$ interlayer coupling and results in a large biaxial anisotropy.

To sum up, the $CaIrO_3/CaMnO_3$ superlattice shows an unprecedented AMR of ~70%, utilizing two key factors: a strong biaxial anisotropy and a spin-flop metamagnetic transition. Combined control of tilt pattern and superlattice construction is demonstrated to optimize the bi-axial magnetic anisotropy, the interlayer coupling mediated by a thick layer, and the field-pseudospin coupling. All these facets coalesce constructively to maximize the transport anisotropies in 3d-5d superlattices. This proof-of-concept study is set to introduce new avenues for designing highly sensitive AMR readout devices for emerging AFM spintronics.

References

[1] P. Němec, M. Fiebig, T. Kampfrath, & A. V. Kimel, *Antiferromagnetic opto-spintronics.* Nat. Phys.14, 229 (2018).
[2] L. Šmejkal, Y. Mokrousov, B. Yan, & A. H. MacDonald, Nat. Phys.14, 242 (2018).
[3] T. Jungwirth, J. Sinova, A. Manchon, X. Marti, J. Wunderlich, & C. Felser, Nat. Phys.14, 200 (2018).
[4] M. B. Jungfleisch, W. Zhang, & A. Hoffmann, Phys. Lett. A 382, 865 (2018).
[5] V. Baltz, A. Manchon, M. Tsoi, T. Moriyama, T. Ono, & Y. Tserkovnyak, Rev. Mod. Phys. 90, 015005 (2018).
[6] T. Jungwirth, X. Marti, P. Wadley, & J. Wunderlich, Nat. Nano. 11, 231 (2016).
[7] W. Witczak-Krempa, G. Chen, Y. B. Kim, L. Balents, Annu. Rev. Condens. Matter Phys.5, 57 (2014).
[8] J. G. Rau, E. K.-H. Lee & H.-Y. Kee, Annu. Rev. Condens. Matter Phys. 7, 195 (2016).
[9] L. Zhang, B. Pang, Y. B. Chen, & Y. Chen, Crit. Rev. Solid State Mater. Sci. 43, 367 (2018).
[10] M. Masuko, J. Fujioka, M. Nakamura, M. Kawasaki, & Y. Tokura, APL Mater. 7, 081115 (2019).

[11] K. Huang, L. Wu, M. Wang, N. Swain, M. Motapothula, Y. Luo, K. Han, M. Chen, C. Ye, A. J. Yang, H. Xu, D. C. Qi, A. T. N'Diaye, C. Panagopoulos, D. Primetzhofer, L Shen, P. Sengupta, J. Ma, Z. Feng, C. W. Nan, & X. R. Wang, Appl. Phys. Rev. **7**, 011401 (2020).
[12] D. Yi, J. Liu, S. L. Hsu, L. Zhang, Y. Choi, J. W. Kim, Z. Chen, J. D. Clarkson, C. R. Serrao, E. Arenholzh, P. J. Ryan, H. Xu, R. J. Birgeneau, & R. Ramesh, Proc. Natl. Acad. Sci. U.S.A. **113**, 6397. (2016).
[13] Z. S. Lim, C. Li, X. Chi, G. J. Omar, H. H. Ma, Z. Huang, S. Zeng, P. Yang, T. Venkatesan, A. Rusydi, S. J. Pennycook, & A. Ariando, Nano Lett. **20**, 1890 (2020).
[14] A. M. Glazer, Acta. Cryst. **B28**, 3384 (1972).
[15] A. M. Glazer, Acta. Cryst. **A31**, 756-762 (1975).
[16] See Supplemental Material for additional information
[17] Z.S. Lim, C. Li, Z. Huang, X. Chi, J. Zhou, S. Zeng, G. J. Omar, Y. P. Feng, A. Rusydi, S. J. Pennycook, T. Venkatesan, and A. Ariando, Small **16**, 2004683 (2020).
[18] J. Nichols, X. Gao, S. Lee, T. C. Meyer, J. W. Freeland, V. Lauter, D. Yi, J. Liu, D. Haskel, J. R. Petrie, E. J. Guo, A. Herklotz , D. Lee, T. J. Ward, G. Eres, M. R. Fitzsimmons, & H. N. Lee, Nat. Comms.**7**, 12721 (2016).
[19] J. Matsuno, K. Ihara, S. Yamamura, H. Wadati, K. Ishii, V. V. Shankar, H. Y. Kee, & H. Takagi, Phys. Rev. Lett.**114**, 247209 (2015)
[20] J. B. Goodenough, Phys. Rev. **100**, 564 (1955)
[21] R. K. Sahu, Z. Hu, M. L. Rao, S. S. Manoharan, T. Schmidt, B. Richter, M. Knupfer, M. Golden, J. Fink, & C. M. Schneider, Phys. Rev. B **66**, 144415 (2002).
[22] H. L. Feng, M. P. Ghimire, Z. Hu, S. C. Liao, S. Agrestini, J. Chen, Y. Yuan, Y. Matsushita, Y. Tsujimoto, Y. Katsuya, M. Tanaka, H. J. Lin, C. T. Chen, S. C. Weng, M. Valvidares, K. Chen, F. Baudelet, A. Tanaka, M. Greenblatt, L. H. Tjeng, & K. Yamaura, Phys. Rev. Materials **3**, 124404 (2019).
[23] E. Shimshoni, N. Andrei & A. Rosch, Phys. Rev. B **68**, 104401 (2005).
[24] P. Orgiani, A. Galdi, C. Aruta, V. Cataudella, G. D. Filippis, C. A. Perroni, V. M. Ramaglia, R. Ciancio, N. B. Brookes, M. M. Sala, G. Ghiringhelli, & L. Maritato, Phys. Rev. B **82**, 205122 (2010).
[25] D. H. Kim, S. M. Lee, S. Kolesnik, B. Dabrowski, B. –G. Park, J. –Y. Kim, J. Lee, B. I. Min, & J. –S. Kang, J. Appl. Phys. **107**, 09E137 (2010).
[26] S. Pal, S. Govinda, M. Goyal, S. Mukherjee, B. Pal, R. Saha, A. Sundaresan, S. Jana, O. Karis, J. W. Freeland, & D. D. Sarma, Phys. Rev. B **97**, 165137 (2018).
[27] M. A. Laguna-Marco, P. Kayser, J. A. Alonso, M. J. Martínez-Lope, M. V. Veenendaal, Y. Choi, & D. Haskel, Phys. Rev. B **91**, 214433 (2015).
[28] A. Minguzzi, O. Lugaresi, E. Achilli, C. Locatelli, A. Vertova, P. Ghigna, & S. Rondinini, Chem. Sci. **5**, 3591 (2014).
[29] L. Vistoli, W. Wang, A. Sander, Q. Zhu, B. Casals, R. Cichelero, A. Barthélémy, S. Fusil, G. Herranz, S. Valencia, R. Abrudan, E. Weschke, K. Nakazawa, H. Kohno, J. Santamaria, W. Wu, V. Garcia, & M. Bibes., Nat. Phys. **15**, 67 (2019).
[30] B. R. K. Nanda, S. Satpathy, & M. S. Springborg, Phys. Rev. Lett. **98**, 216804 (2007).

[31] C. He, A. J. Grutter, M. Gu, N. D. Browning, Y. Takamura, B. J. Kirby, J. A. Borchers, J. W. Kim, M. R. Fitzsimmons, X. Zhai, V. V. Mehta, F. J. Wong, & Y. Suzuki, Phys. Rev. Lett. **109**, 197202 (2012).
[32] P. Pandey, R. Rana, & D. S. Rana, Europhys. Lett. **109**, 38005 (2015).
[33] P. Pandey, T. Das, R. Rana, J. B. Parmar, S. Bhattacharyya, & D. S. Rana, Nanoscale **7**, 3292 (2015).
[34] S. Vélez, V. N. Golovach, A. Bedoya-Pinto, M. Isasa, E. Sagasta, M. Abadia, C. Rogero, L. E. Hueso, F. S. Bergeret, & F. Casanova, Phys. Rev. Lett. **116**, 016603 (2016).
[35] G. Peramaiyan, R. Sankar, I. P. Muthuselvam, & W. –L. Lee, Sci. Rep. **8**, 6414 (2018).
[36] T. S. Suraj, G. J. Omar, H. Jani, M. M. Juvaid, S. Hooda, A. Chaudhuri, A. Rusydi, K. Sethupathi, T. Venkatesan, A. Ariando, & M. S. R. Rao, Phys. Rev. B **102**, 125145 (2020).
[37] H. Nakayama, M. Althammer, Y. –T. Chen, K. Uchida, Y. Kajiwara, D. Kikuchi, T. Ohtani, S. Geprägs, M. Opel, S. Takahashi, R. Gross, G. E. W. Bauer, S. T. B. Goennenwein, & E. Saitoh, Phys. Rev. Lett. **110**, 206601 (2013).
[38] P. Wadley, B. Howells, J. Železný, C. Andrews, V. Hills, R. P. Campion, V. Novák, K. Olejník, F. Maccherozzi, S. S. Dhesi, S. Y. Martin, T. Wagner, J. Wunderlich, F. Freimuth, Y. Mokrousov, J. Kuneš, J. S. Chauhan, M. J. Grzybowski, A. W. Rushforth, K. W. Edmonds, B. L. Gallagher, & T. Jungwirth, Science **351**, 587 (2016).
[39] N. Lee, E. Ko, H. Y. Choi, Y. J. Hong, M. Nauman, W. Kang, H. J. Choi, Y. J. Choi, & Y. Jo, Adv. Mater.**30**, 1805564 (2018).
[40] H. Wang, C. Lu, J. Chen, Y. Liu, S. L. Yuan, S. W. Cheong, S. Dong, & J. M. Liu, Nat. comms. **10**, 2280 (2019).
[41] H. Liu, & G. Khaliullin, Phys. Rev. Lett. **122**, 057203 (2019).
[42] J. Porras, J. Bertinshaw, H. Liu, G. Khaliullin, N. H. Sung, J. –W. Kim, S. Francoual, P. Steffens, G. Deng, M. M. Sala, A. Efimenko, A. Said, D. Casa, X. Huang, T. Gog, J. Kim, B. Keimer, & B. J. Kim, Phys. Rev. B **99**, 085125 (2019).
[43] J. W. Kim, Y. Choi, J. Kim, J. F. Mitchell, G. Jackeli, M. Daghofer, J. V. Brink, G. Khaliullin, & B. J. Kim, Phys. Rev. Lett. **109**, 037204 (2012).
[44] Y. F. Nie, P. D. C. King, C. H. Kim, M. Uchida, H. I. Wei, B. D. Faeth, J. P. Ruf, J. P. C. Ruff, L. Xie, X. Pan, C. J. Fennie, D. G. Schlom, & K. M. Shen, Phys. Rev. Lett. **114**, 016401(2015).
[45] I. Fina, X. Marti, D. Yi, J. Liu, J. H. Chu, C. Rayan-Serrao, S. Suresha, A. B. Shick, J. Zˇelezny´, T. Jungwirth, J. Fontcuberta, & R. Ramesh, Nat. Comms. **5**, 4671 (2014).
[46] T. Wu, C. H. Wang, G. Wu, D. F. Fang, J. L. Luo, G. T. Liu, & X. H. Chen, J. Phys.: Condens. Matter **20,** 275226 (2008).
[47] D. S. Rana, D. G. Kuberkar, & S. K. Malik, Phys. Rev. B **73**, 064407 (2006).
[48] R. Mahendiran, A. Maignan, S. Hebert, C. Martin, M. Hervieu, B. Raveau, J. F. Mitchell, & P. Schiffer, Phys. Rev. Lett. **89**, 286602 (2002).
[49] J. Klarbring, & S. I. Simak, Phys. Rev. B **97**, 024108 (2018).

Acknowledgements

D.S.R. thanks the Department of Science and Technology (DST) Nanomission for financial support under research project No. SM/NM/NS-84/2016 and the Science and Engineering Research Board (SERB) Technology, New Delhi under the project no. EMR/2016/003598. M.V. acknowledges the DST, India for the INSPIRE faculty award (DST/INSPIRE/04/2017/003059). XAS measurements were performed at UC San Diego in a search for materials for new spin-torque oscillators conducted by Quantum Materials for Energy Efficient Neuromorphic Computing, an Energy Frontier Research Center funded by the U.S. Department of Energy (DOE), Office of Science, Basic Energy Sciences (BES) under Award # DE-SC0019273. This research used resources of the Advanced Photon Source (29ID for soft XAS and 4-ID-D for hard XAS), a U.S. Department of Energy (DOE) Office of Science User Facility operated for the DOE Office of Science by Argonne National Laboratory under Contract No. DE-AC02-

06CH11357; with additional support by National Science Foundation under Grant no. DMR-0703406. Extraordinary facility operations were supported in part by the DOE Office of Science through the National Virtual Biotechnology Laboratory, a consortium of DOE national laboratories focused on the response to COVID-19, with funding provided by the Coronavirus CARES Act. Authors thank Mr. G. L. Prajapati and Mr. Manoj Prajapat for their help in performing magnetization, transport and X-ray diffraction characterizations as well as R. Aniol for TEM specimen preparation. Furthermore, the use of the HZDR Ion Beam Center TEM facilities and the funding of TEM Talos by the German Federal Ministry of Education of Research (BMBF; grant No. 03SF0451) in the framework of HEMCP are acknowledged.

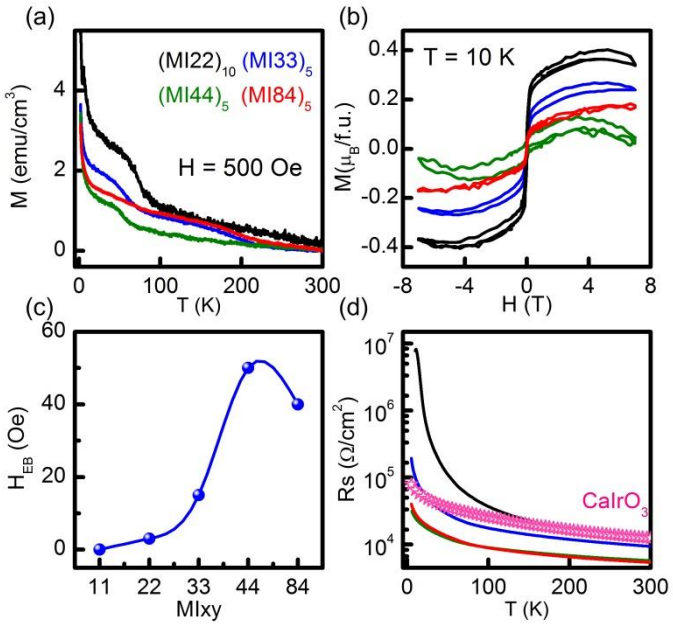

Fig. 1 (a) Temperature and (b) field dependence of magnetization and (c) The strength of exchange bias field with the varying stacking of $CaMnO_3$ and $CaIrO_3$ layers in the (MIxy) superlattices. (d) Sheet resistance as a function of temperature for $(MIxy)_z$ (x = y = 2-4) along with $(MI84)_5$ to elucidate the effect of a larger $CaMnO_3$ period.

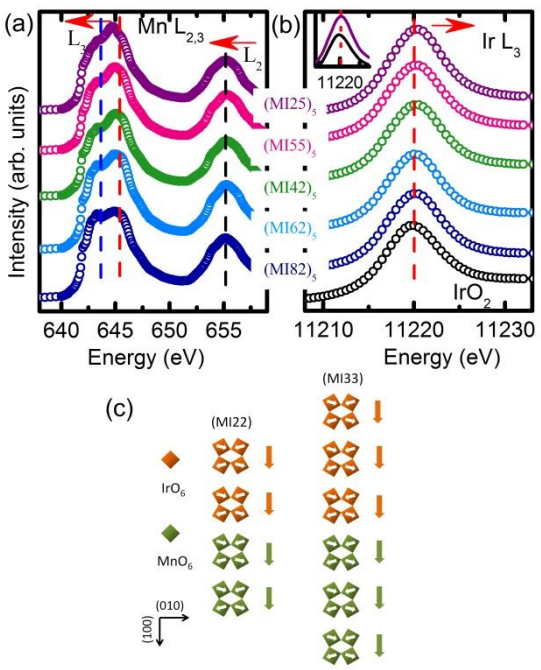

Fig. 2 X-ray absorption spectra around (a) the Mn $L_{2,3}$ edge and (b) Ir L_3-edge for $(MIxy)_z$ superlattices. The insets depict the comparison of the $(MI25)_5$ sample with the IrO_2 reference. (c) Schematic illustrating the spin canting in $CaIrO_3$ and $CaMnO_3$ layers. Here, BO_6 planes for $CaIrO_3$ and $CaMnO_3$ layers are presented in 'ab' plane (or in-plane). These planes are stacked along [001] but for the sake of brevity the top view of the canted moments and net magnetic moment is presented along two in-plane [010] and [100] directions, with reference to pseudo-cubic STO (100) substrate. The length of the arrows showing net magnetic moment does not represent the relative size of the magnetic moment in $CaIrO_3$ or $CaMnO_3$ layers.

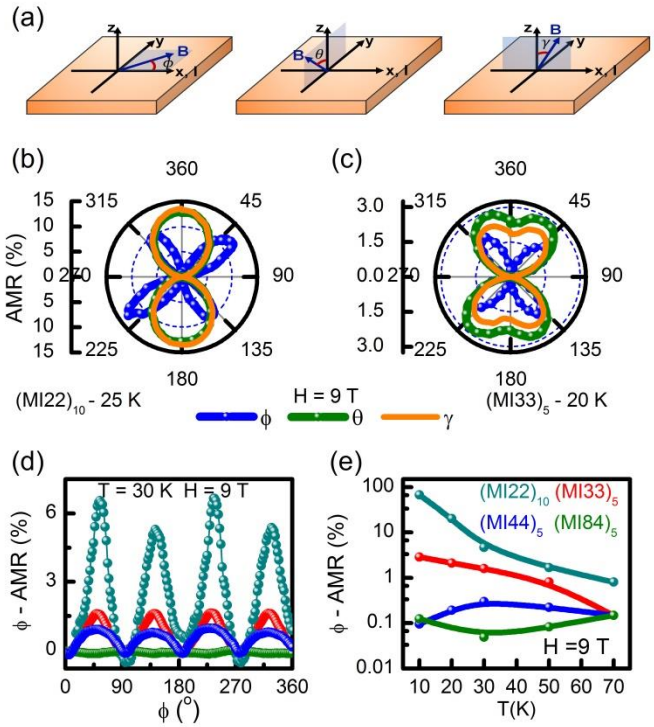

Fig. 3 (a) Schematic illustration of three different rotational geometries to measure the AMR. Polar plots comparing ϕ, θ, and γ-AMRs for (b) $(MI22)_{10}$ and (c) $(MI33)_5$ superlattices. (d) Variation in ϕ-AMR at 30 K for $(MIxy)_z$ (x = y = 2-4) and $(MI84)_5$ (e) Variation in the ϕ-AMR amplitude as a function of temperature for H = 9 T.

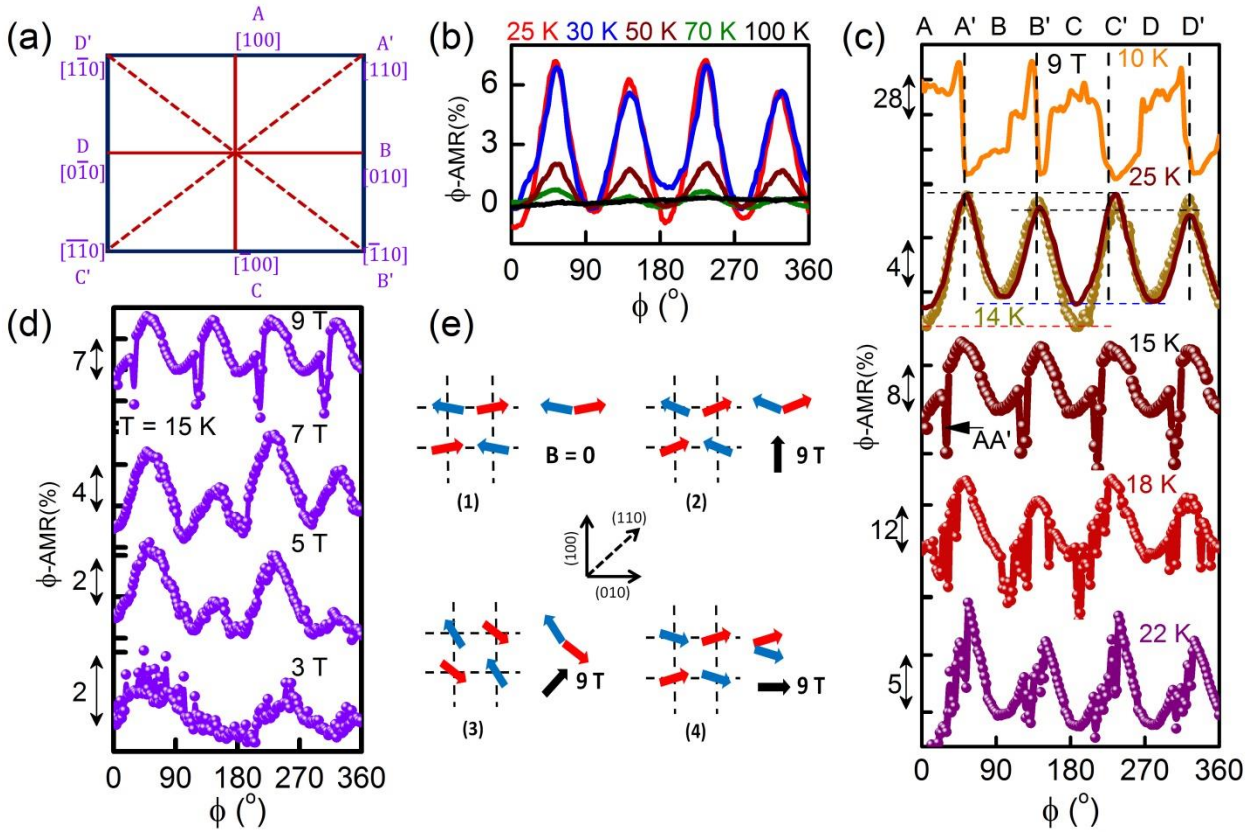

Fig. 4 (a) <*100*> crystallographic in-plane family of directions are labeled as A, B, C, and D and the <*110*> family as A′, B′, C′, and D′. (b) ϕ-AMR for $(MI22)_{10}$ measured at various temperatures in the range of 25 – 100 K at H = 9 T. c) ϕ-AMR of the $(MI22)_{10}$ in the temperature range of 10–20 K for H = 9 T, manifesting the onset of the spin-flop transition at 22 K evident from the additional four-fold symmetry in ϕ-AMR. (d) Field dependence of ϕ-AMR for $(MI22)_{10}$ measured at T = 15 K. (e) Spin arrangement as perceived in relation to the AMR. Spins indicated in two colors (red and blue) correspond to two sublattices of the AFM order. A canting in AFM order at B=0 increases in a field of 9T along the easy (100) axis [1 and 2]. This effect is subtle when B is applied along (110) hard axis [panel 3]. For B = 9T along (010), the spin-flop arrangement at 10 K is shown in the last panel.